Integrated Phased Array for Scalable Vortex Beam Multiplexing

Yuxuan Chen, Simon Levasseur, Leslie A. Rusch, and Wei Shi

Integrated Phased Array for Scalable Vortex Beam Multiplexing

Yuxuan Chen, Simon Levasseur, Leslie A. Rusch, *Fellow, IEEE, Fellow, Optica* and Wei Shi, *Senior Member, IEEE, Senior Member, Optica*

(Invited Paper)

Abstract—Orbital angular momentum (OAM) modes have low model interactions during fiber propagation at data center distances, and thus are suitable for ultra-high capacity systems at low digital signal processing. Generating OAM modes using free-space setups is useful for proof-of-concept experiments, but is not a scalable solution. We use an optical phased array (OPA) with two-dimensional antennas for on-chip circularly polarized OAM beam generation. Our previous work demonstrated an OAM multiplexer for lower-order modes. In this work, we demonstrate an OAM multiplexer that supports a record of 46 (23 per polarization) simultaneous spatial modes up to OAM order 11. We also improve the crosstalk performance of our multiplexer. We incorporate an intensity tuning capability that substantially improves the OAM quality by enabling a uniform power distribution across the antennas. The worst-case crosstalk for the supported OAM5 to OAM11 are found experimentally to be better than -12 dB, with OAM10 achieving -17.2 dB.

Index Terms—Silicon photonics, orbital angular momentum, space division multiplexing, wavelength-division multiplexing, photonic integrated circuits.

I. INTRODUCTION

SPACE division multiplexing (SDM) has been intensely investigated and discussed in the past decade. The SDM technology can be exploited in parallel with multiplexing techniques in the domain of time, frequency, polarization, and quadrature to linearly scale the transmission capacity [1][2][3]. Each spatial mode in the SDM scheme is an independent data-carrying channel.

Modal multiplexing in a few mode fiber (FMF) offers a high information density for SDM, and can be combined with multi-core fibers to further increase data capacity. Mode coupling occurs within an FMF, so in practice, multi-input multi-output (MIMO) processing is required to resolve this coupling on the receiver side. At data center distances, using orbital angular momentum (OAM) modes can avoid the complexity of MIMO algorithms [4].

Due to a lack of mature integrated solutions, experimental orbital angular momentum (OAM) mode excitation for fibers has used free-space setups. They involve spatial light modulators [5], spiral phase plates [6] or q-plates [7] for beam generation. They require many components for mode size

The authors are with the Department of Electrical and Computer Engineering, Centre for Optics, Photonics and Lasers (COPL), University of Laval, Quebec, QC G1V 0A6, Canada (e-mail: yuxuan.chen.1@ulaval.ca; simon.levasseur@copl.ulaval.ca; leslie.rusch@gel.ulaval.ca; wei.shi@gel.ulaval.ca).

conversion, and polarization management (half wave-plate and quarter wave-plate). Scaling such free-space setups to support a large number of modes is challenging, requiring precise optical alignment, large size and high cost components.

Integrated devices based on ring-resonators [8][9], waveguide surface holographic gratings [10][11] and star couplers [12][13] demonstrated compact OAM generation in non-circular polarization. In [9], two bus waveguides and a ring were used to multiplex four OAM modes. A design that superposes holographic fork gratings [11] to multiplex two linear polarization was experimentally demonstrated to support four OAM modes. In [13] a star coupler based integrated circuit and laser-written 3D waveguides were used to demonstrate 15 multiplexed modes. The theory and performance of these devices are reviewed in [14]. For the next generation transmission systems, a larger number of modes and lower crosstalk are required to accommodate ultra-large capacity.

Our previous work [15] demonstrated 14 OAM modes (7 per circular polarization) using an 17-antenna phased array. We measured a relatively high crosstalk (-6 dB, worst-case) caused by the non-uniform intensity distribution among antennas due to fabrication errors. In this paper, we increase the antenna number to 27 to support higher order OAM modes (up to OAM11) and demonstrate a record of 46 OAM modes (23 per circular polarization). The increased number of antennas improves beam quality. The intensity tuning circuit provides better phase resolution and uniform power distribution across the antennas, substantially improving the OAM quality (worst-case crosstalk -17.2 dB, lowest ever reported on a silicon chip).

We describe our chip design and fabrication in Section II. We present our transfer matrix method based simulation model in Section III. The experimental setups and measurement results for intensity and phase tuning are discussed separately in Section IV and Section V. The verification of OAM generation through interference pattern is in Section VI. We discuss our current limitations in Section VII and we conclude our paper in Section VIII.

II. SILICON PHOTONICS MULTIPLEXER

A. Principal of Operation in brief

A schematic of our device is presented in Fig. 1. Details of the principal of operation can be found in [16], here we provide a brief summary. A single mode fiber (SMF) array inputs data signals to the fiber-to-chip couplers on the left
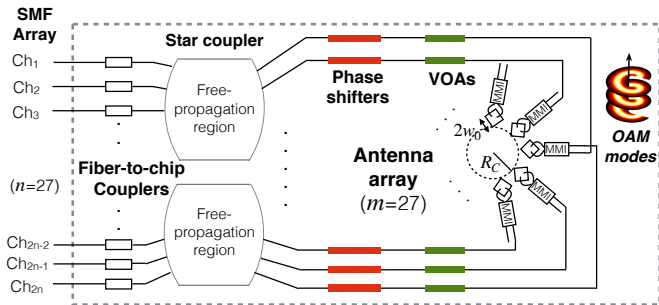
Fig. 1: Schematic of the integrated phased array with $n = 27$ input couplers per polarization and $m = 27$ output antennas.

side of the OAM multiplexer circuit. Each fiber input with data is mapped to a mode and polarization. The OAM modes generated have either right or left circular polarization, ideal for fiber propagation.

We use a star coupler for on-chip phase manipulation to create OAM modes. We have two identical star couplers, one for each circular polarization, left and right. Each 2×2 MMI has one input from each star coupler. The MMIs create 90-degree phase shifts that establish the orthogonality of the polarizations. At the 2-dimensional (2D) antennas the contributions of each MMI combine to produce circularly-polarized beams. The 2D antennas are arranged in a circle whose circumference can be adapted to facilitate coupling to a given fiber.

The OAM modes have azimuthal phase dependency of $exp(jl\Phi)$, where l is the topological charge of the OAM mode. In optical fibers, the electrical field of the OAM modes can be expressed by [17]:

$$E(r, \Phi, z, t) = E(r)e^{jl\Phi}e^{j(\omega t - \beta z)} \qquad (1)$$

where $E(r)$ is the radial mode profile, ω is the angular frequency and β is the propagation constant. Fiber OAM modes are circularly polarized. The integer l represents the OAM order. The sign of l indicates the handedness of the OAM beam.

B. Requirement for tuning

The star coupler design leads to inherent differences in amplitude at each output. Fabrication errors in the MMIs and 2D antennas could also contribute to amplitude variations. In addition, variations in both thickness and width for waveguide paths could be on the order of 10 nm. This leads to phase error as high as 2π radians for our centimeter scale circuits.

We use tuners to compensate for imperfections in component design and in fabrication. In Fig. 1 we indicate the phase shifters and variable on-chip attenuators (VOAs) that are placed at each output of the star couplers. The phase and amplitude of each output can be adjusted independently to improve the quality of the OAM beams generated.

We have previously examined the impact of phase deviations, and demonstrated the correction attainable with tunable phase shifters [15]. However, the non-uniformity of the intensity at outputs also limits system performance in two ways.

First it deforms the output OAM beam. Secondly, it diminishes our ability to tune the phase as the phase errors are masked by amplitude effects.

C. Fabricated chip

Our device was fabricated at Advanced Micro Foundry Inc through CMC Microsystems. A top view of the fabricated chip is shown in Fig. 2a. In the scanning electron microscope (SEM) image (Fig. 2b), we see the array of 2D antennas evenly-spaced with central axis pointing toward the center of the circumference. Each 2D antenna is connected to a 2×2 MMI through $5\mu m$ bents. The 2×2 MMI creates ±90 degree phase difference between two linear polarization inputs (quasi-TE modes in our design), enabling on-chip circularly polarized beam generation. A magnified view at $50°$ tilt of one 2D antenna is shown in Fig. 2c, where the square around the grating region is the shallow-etched silicon layer at $150\mu m$ thickness.

We generated up to OAM4 in our previous demonstration with a 17 antenna array [15]. In this design, we increase the antenna number to 27. The device should support up to OAM order 13 but we were unable to verify experimentally. Thus we demonstrate up to OAM of order 11 with our measured results. The directional coupler in [15] is replaced with the 2×2 MMI of the same functionality. The MMIs are more compact and less sensitive to fabrication compare to directional couplers.
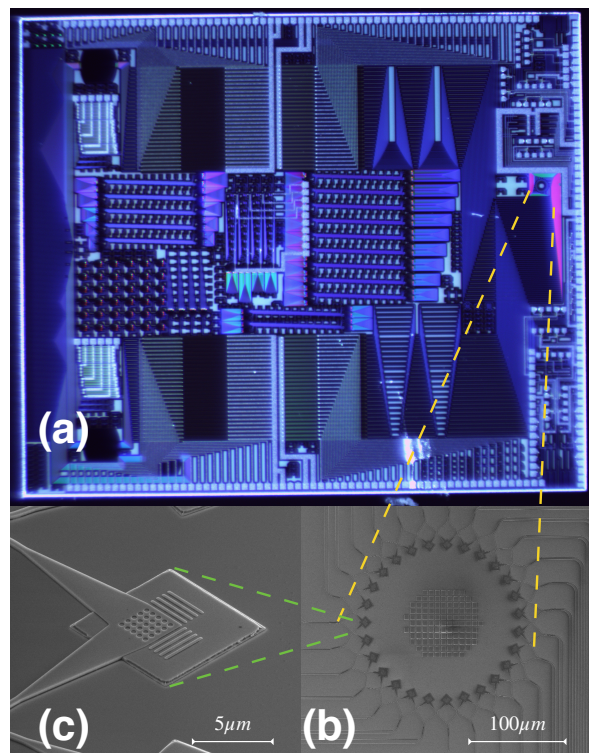

Fig. 2: Photograph of (a) the fabricated device, and scanning electron microscope images of (b) the antenna array, and (c) one 2D antenna.

III. Modeling and Tuning

We use simulation to probe the impact of amplitude and phase errors. Our previous simulations for phase tuning [16] did not include star coupler imperfections that affect output amplitude variations, hence we explain here the updated simulation model. We describe simulation of the limitations of our tuning feedback loop.

A. Updated simulation model

Details of our previous simulation model for on-chip signals and the free-space output beam can be found in [16]. We used the transfer matrix method to model the electrical fields produced at each antenna output. We modeled the formation of the OAM beam in the far field by propagating a Gaussian beam from each antenna output using the electrical field found from the transfer matrix method. Here we describe our original transfer matrix and how it is updated to include amplitude variations in the star coupler.

Let q be an index for the input port (one index for a given mode order and circular polarization orientation), and p be an index for the output port, i.e., the 2D antennas. The total transfer matrix (elements $t_{p,q}$) for all on-chip components is found by multiplying the transfer matrices in sequence. For generation of left circular polarization we previously found

$$t_{p,q} = -\eta_q \cdot \frac{i}{2} \begin{pmatrix} 1 \\ i \end{pmatrix} \cdot e^{-i\theta_p} \cdot \frac{e^{i\varphi_{p,q}}}{\sqrt{m}} \qquad (2)$$

A similar result holds for right circular polarization.

The first term in (2) is from the fiber-to-chip coupler efficiency, η_q. The directional coupler offers a 50/50 power splitting ratio and $\pm 90°$ phase difference, contributing the next term. The 2D antenna located at an angle of θ_p contributes the third term. The star coupler was idealized in the denominator of the final term with an amplitude that does not depend on p or q.

We now modify the transfer matrix contribution from the star couplers to account for amplitude $\eta_{p,q}$ that varies, using the model in [18]. We take θ_1 to be the reference zero phase. With this notation $\eta_{(m+1)/2,q}$ will see the highest amplitude, while the smallest amplitude occurs at either $\eta_{1,q}$ or $\eta_{m,q}$. The amplitudes $\eta_{p,q}$ follow a Gaussian distribution in p. The variance of the Gaussian shape is determined by the physical geometry of the star coupler.

The updated transfer matrix term is

$$\hat{t}_{p,q} = -\eta_q \cdot \frac{i}{2} \begin{pmatrix} 1 \\ i \end{pmatrix} \cdot e^{-i\theta_p} \cdot \frac{e^{i\varphi_{p,q}}}{\sqrt{\eta_{p,q}m}} \qquad (3)$$

B. Fabrication errors and tuning

We incorporate into the simulation model a term to take into effect fabrication errors. We also model the effect of phase and amplitude corrections from tuning. Let $\Delta\varphi_{p,q}$ be the cumulative phase error on path p,q introduced by all fabrication errors.

We apply amplitude and phase correction only on the output paths. Therefore correction terms are only indexed by p. For path p, let α_p be the attenuation and $\bar{\varphi}_p$ the phase adjustment.

The transfer matrix accounting for fabrication errors and tuning becomes

$$\tilde{t}_{p,q} = -\eta_q \cdot \frac{i}{2} \begin{pmatrix} 1 \\ i \end{pmatrix} \cdot e^{-i\theta_p} \cdot \frac{e^{i\varphi_{p,q}}}{\sqrt{\eta_{p,q}m}} \cdot e^{i\Delta\varphi_{p,q}} \cdot \alpha_p \cdot e^{i\bar{\varphi}_p} \qquad (4)$$

IV. Intensity Uniformity across Antennas

Several OAM generators use vertical emission in a phased array with circular geometry. Uniformity of intensity across the emission affects the purity of the generated OAM modes. In [19] the omega shaped bus waveguide delivers monotonically increasing intensities to the gratings emitters. In star couplers the intensity non-uniformity is an artefact of the light splitting, as well as fabrication uncertainties [13]. No compensation measures have been demonstrated for circular phased arrays, despite intensity non-uniformity limiting performance.

A. Simulation of performance impact of non-uniformity

For a multiplexer, the crosstalk is the most relevant performance metric. Both phase error and non-uniform intensity across emitters contribute to crosstalk. We model the phase errors $\Delta\varphi_{p,q}$ as independent and identically distributed, with a uniform distribution from zero to $\Delta\varphi_{max}$. We consider $10°$, $30°$, and $50°$ for $\Delta\varphi_{max}$.

Let $I_{p,q}$ be the intensity at antenna p when generating mode with index q. The amplitude variation is captured by $\eta_{p,q}$ in our updated model. The spread of intensities for mode q is

$$\Delta I_q = \frac{\max_p I_p - \min_p I_p}{\max_p I_p} = \frac{\eta_{\frac{m+1}{2},q} - \min(\eta_{1,q}, \eta_{m,q})}{\eta_{\frac{m+1}{2},q}} \qquad (5)$$

For our design, $0.35 < \Delta I_q < 0.45$.

Now suppose that one mode is incident on the chip acting as a demultiplexer. Let P_i be the power on the output port associated with input mode i, and P_q the power on another output port, i.e., $q \neq i$. The crosstalk between modes i and q is the ratio of these powers. Bit error rate performance for mode i is dominated by the worst case crosstalk among all crosstalk contributions $q \neq i$.

The crosstalk varies with phase error (parameterized by $\Delta\varphi_{max}$) and nonuniform intensity (parameterized by ΔI). The expected worst case crosstalk is

$$XT(\Delta\varphi_{max}, \Delta I_q) = \max_{q \neq i} \frac{E(P_q)}{E(P_i)} \qquad (6)$$

where the expectation E is taken over the uniformly distributed phase error. We estimate the expectation in Monte Carlo simulations.

We excite one OAM mode with an ideal chip ($\Delta\varphi_{p,q}=0$ and $\Delta I = 0$). We simulate $i = 0$ corresponding to OAM0 in left circular polarization. We simulate a non-ideal chip demultiplexing the ideal incident signal. In our simulations we sweep ΔI to quantify the impact of intensity non-uniformity for various star coupler designs. For our fabricated chip, $\Delta I = 0.35$ at OAM0.

We plot the expected worst case crosstalk in Fig. 3. The ideal intensity uniformity is $\Delta I = 0$, where all curves find
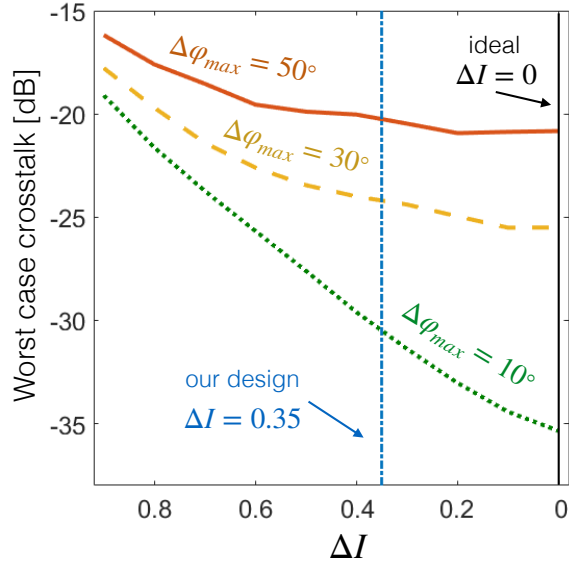
Fig. 3: Simulated worst case crosstalk at OAM0 vs. intensity non-uniformity, for three levels of phase error.

the smallest worst case crosstalk for a given phase error. As expected, a larger phase error variance leads to larger worst case crosstalk.

For our experimental setup, even when using heaters to tune the phase correction, we expect the largest phase error to be 10°, corresponding to the green dotted line. Tuning from the ΔI of our design to the ideal value of zero would lead to a 3 dB improvement in worst case crosstalk at that phase error.

Even at ideal intensity uniformity, residual phase error can be devastating. Crosstalk degradation is over 15 dB for the phase error cases simulated. There will always exist the practical challenge to jointly optimize the intensity and phase correction. Better intensity uniformity will allow us to better reduce residual phase error, as crosstalk is lower and we have better visibility to improve phase tuning.

B. Experimental setup to examine impact of non-uniformity

Our experimental setup for intensity tuning is shown in Fig. 4. The shaded components are not used in this particular experiment. Their purpose will be explained in later discussions as they become relevant. They are part of a free-space cage system for alignment of components, therefore, all elements in the cage system are included in each setup description.

The chip is used in the multiplexer configuration. We send a continuous wave signal on one fiber input to generate a single OAM beam. For this measurement OAM0 is generated. The blue line traces the path of the OAM beam to a camera that captures the intensity profile of the emitter array. For intensity tuning, we use a 4-f system to provide five times magnification. This improves the sensitivity of the camera to isolate power from specific emitters. Lens L1 has a 10 mm focal length and L2 a 50 mm focal length.

C. Results of tuning to correct non-uniformity

On the magnified images from the camera, we identify regions for each antenna position. We integrate the power across each region to estimate I_p. We identify the minimum I_p and tune the VOAs independently targeting this intensity at each of the 26 other antennas. The maximum attenuation is 6 dB and the tuning steps are 0.2 dB. The response to tuning is nonlinear and sensitive to small adjustments.

Figure 5a shows the measured intensity I_p at antenna p before tuning in blue solid line. The intensity is not smooth due to process variations in the 2D antennas and MMIs. We fit measured data to the Gaussian shape from our updated model. The maximum intensity in the fitted curve is normalized to one. The fitted curve has $\Delta I = 0.33$, very close to the modeled $\Delta I = 0.35$. The raw measured intensity has $\Delta I = 0.41$.

Ideal tuning would attenuate the paths to achieve $I_p = 0.65$ for all antennas. While total emitted power is reduced, the intensity would be uniform. Following the VOA tuning the intensity we measure is the dashed red line in Fig. 5a. It is observably more uniform, with $\Delta I = 0.28$.

Our attenuation is highly nonlinear with applied voltage. For example, see the behavior at antenna 15. An additional voltage change equivalent to 0.2 dB attenuation resulted in complete extinction of the antenna output. We see that antennas 5, 16 and 24 show no attenuation and we suspect the wire bonding
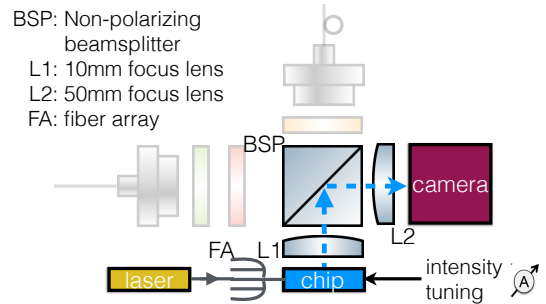

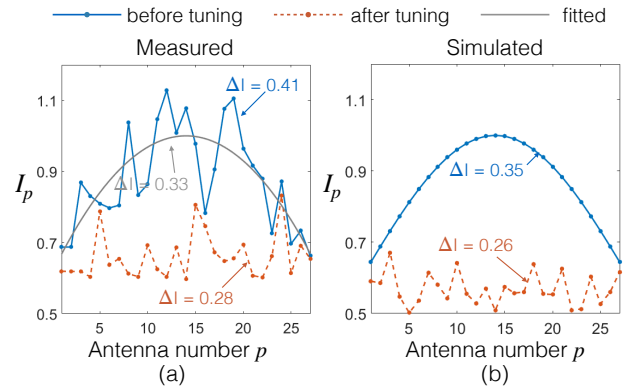Fig. 4: Experimental setup for intensity tuning based on the near-field chip output in free-space.

Fig. 5: Normalized intensity per antenna for OAM0 mode a) measured and (b) simulated. Before tuning in solid blue curves, after tuning in dashed red curves, fitted distribution in solid gray curve.

is broken on these paths.

We calculate statistics of the tuned intensity profile vis-a-vis the desired constant value of $\min I_p$, both bias and variance. In simulation, the intensity tuning error is modeled as a Gaussian error with the experimental bias and variance. The three data points with broken wire bonds were excluded in our calculation of tuning error statistics.

Figure 5b shows the simulated intensity I_p at antenna p in blue solid line, with maximum intensity normalized to one. It has a Gaussian shape that for OAM0 yields $\Delta I = 0.35$. The curve in red shows typical intensity after tuning assuming a tuning error parameterized by what we experienced experimentally. The intensity excursion is again clearly reduced. When simulating over 1e5 tuning error realizations, we calculated an average intensity spread of $\Delta I = 0.26$.

Despite challenges in our tuning apparatus, we are able to reduce the intensity non-uniformity. Consulting the crosstalk behaviour simulation in Fig. 3, the initial $\Delta I = 0.41$ has a spread of 9.4 dB between red and green curves, while the final $\Delta I = 0.28$ has a spread of 11.4 dB. This will aid in phase tuning while observing crosstalk. Also, the worst case error is improved by 2 dB when phase is tuned to only 10° error. We will see in later sections that we achieved a 3.3 dB improvement in worst case crosstalk experimentally.

V. PHASE TUNING WITH MORE UNIFORM INTENSITY

We conduct phase tuning with and without the optimized intensity profile described in the previous section. The chip demultiplexes an OAM mode generated off chip with a vortex plate. We correct phase error to minimize the measured crosstalk.

A. Experimental setup for phase tuning

We use the cage system to couple light onto our chip and observe power of the output array of SMF antennas, i.e., a demultiplexer configuration. As seen in Fig. 6, a Gaussian free-space beam (red dashed) with circular polarization passes from the collimator to a vortex plate. The vortex plate has half-wave retardance to create an anti-aligned (AA) OAM of order l. The free-space beam is coupled onto the fabricated chip. The OAM mode is then de-multiplexed by our device into 27 OAM modes (-13 to 13 order), each converted to fundamental mode and output to a power meter. The power that goes to the OAM order l (anti-aligned) is intended. The power to other modes creates crosstalk.

For phase tuning, we generate left circular OAM10 and monitor power at each of the 27 power meters for outputs of left circular OAM modes. We continuously monitor power while applying phase tuning to minimize the worst-case crosstalk. We use a gradient descent algorithm to find the optimum tuning. The metal heaters, 750 nm above the routing waveguides, increase the local temperature when tuned, changing the effective index and phase. The routing waveguides are 65 μm apart so the thermal crosstalk is negligible.

As we sweep the tuning signal, the phase in the tuning path change continuously, while the phase in all other paths is not influenced. The power at the output fibers (determined by the interference of all paths) follows a sinusoidal trend as the tuning signal is swept. We can tune over a 2π phase change. Details of the phase tuning procedure are provided in the appendix A.

B. Phase tuning results

We assess performance via histograms for the crosstalk (XT) on OAM10 from the 26 non-target output ports we monitored. For each histogram we note the average crosstalk, as well as the worst case crosstalk (the right-most crosstalk level in the histogram). In Fig. 7a we show the histogram of crosstalk in dB with no tuning (neither amplitude nor phase). In Fig. 7b we show the histogram when tuning only phase, and in Fig. 7c when tuning both amplitude and phase.

The average crosstalk is as high as -3.9 dB for the bare chip, with no tuning to correct errors. The worst case crosstalk is 2.4 dB, with some modes having more power than the target mode. When correcting phase alone, we are able to suppress unwanted modes. The histogram in Fig. 7b is shifted left, with worst case crosstalk improved to -13.9 dB. When tuning both amplitude and phase the average crosstalk in Fig. 7c is -20.3 dB. The worst case crosstalk of -17.2 dB is the lowest crosstalk ever demonstrated with SOI based OAM multiplexer.

Clearly tuning is essential. The phase variations are the most critical, with the greatest improvement coming from phase correction. The combination of amplitude and phase tuning gives another 3 dB performance enhancement. The crosstalk is low enough for use in spatial demultiplexing systems.

In Fig. 7d we show the crosstalk on OAM 10 for each mode once the tuning is optimized. This is the data that was used to create the histogram in Fig. 7c. We see that there is no discernible trend in the crosstalk with particular modes. Neither neighboring modes or much lower order modes show any particular crosstalk behavior.

C. Crosstalk matrix with optimal tuning

The previous section examined the performance for OAM10, the same mode that was used for tuning. Next we examine the performance of other modes, while leaving the tuning signals unchanged. We note that higher order modes are more likely to be exploited in spatial division multiplexing [4], as they offer lower crosstalk and more stability. We replace
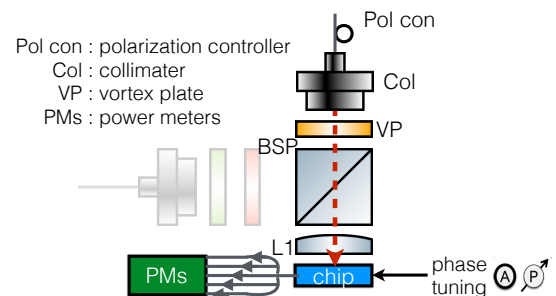

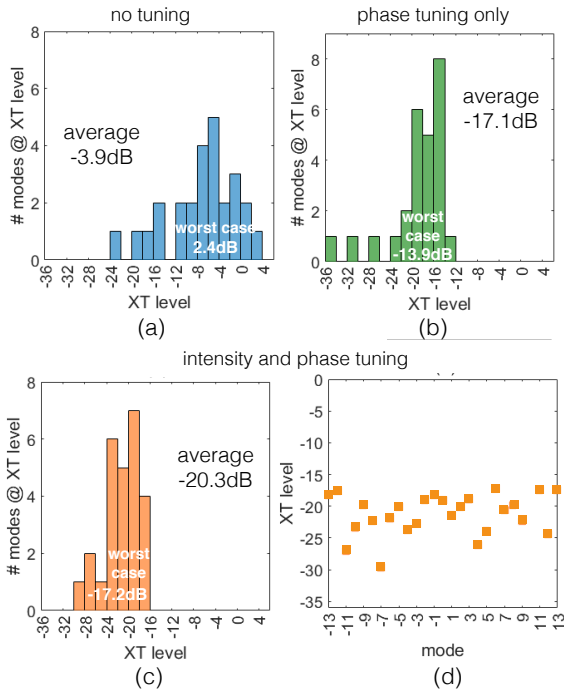Fig. 6: Experimental setup for phase tuning and crosstalk measurement, device working as demultiplexer.

Fig. 7: Histograms of crosstalk per mode for target mode OAM10: (a) without tuning, (b) with only phase tuning, (c) with intensity and phase tuning, and (d) crosstalk per mode at the optimal tuning.
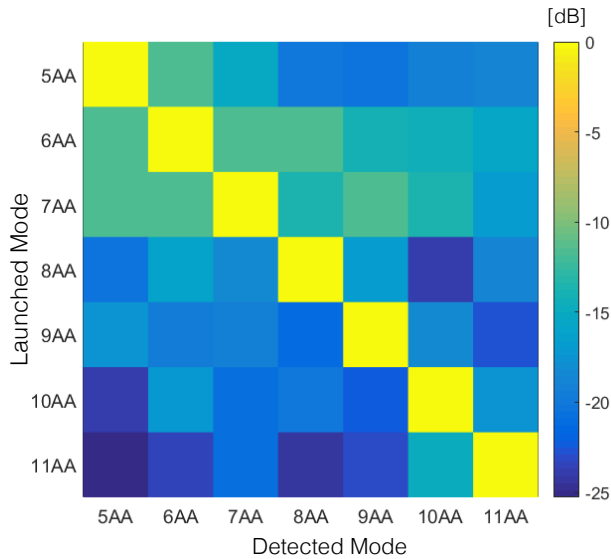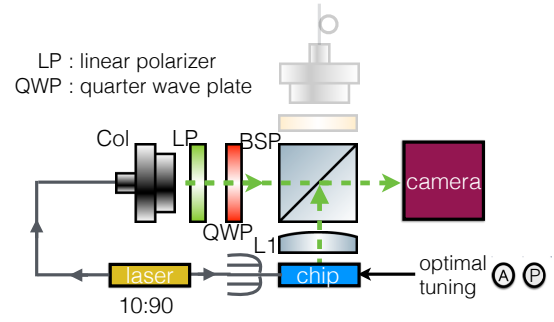

Fig. 9: Experimental setup for interferogram measurement.

the worst case crosstalk for these modes is around -12 dB. The discrepancy in performance over modes is due to the variations in size of the beam projected on the chip. Each OAM mode exhibits divergence with a rate that varies with mode order. Our system is optimized for OAM10, and high order modes have similar divergence. Therefore these modes have better mode matching with the antenna array. We expect uniform performance in appropriate OAM fiber coupling. Such coupling would involve short free-space propagation length and negligible divergence.

VI. OAM SPIRAL INTERFERENCE PATTERNS

We performed the tuning optimization described in the previous section at 1540 nm. With the tuning fixed at this optimized setting, we next examine the bandwidth of our multiplexer. We turn to interference spirals as a means of confirming good OAM generation.

A. Experimental setup for interference pattern

An interferogram between an OAM beam and a reference Gaussian of the same polarization will yield a spiral intensity patter. The number of nested spirals indicates the order of the OAM mode. In Fig. 9 we present our setup for interferogram measurements. The beam generated by our device is collimated by L1. A reference Gaussian is circularly polarized after passing through a polarizer and a quarter waveplate. The generated beam and the reference Gaussian propagate co-linearly on the right side of the beam splitter. The interferogram is captured on the camera (dashed green line).

In the appendix we provide interferograms of many modes at 1540 nm. Given the constraints of our experimental setup (lenses, spot sizes, divergence, etc.), the clearest interferograms are produced for OAM-5. Therefore, we focus on the OAM-5 interferograms as we sweep the laser wavelength over C-band to demonstrate bandwidth.

B. Results of interferogram measured at multiple wavelengths

Interference patterns for OAM-5 measured from 1530 nm to 1565 nm are presented in Fig. 10. The origins of the spirals have high power and appear dark red in the center of the image. The arms follow, in number equal to the OAM

Fig. 8: Measured crosstalk matrix for 5AA to 11AA.

the vortex plate in the setup, examining in turn orders $l =$5 to 11.

For each anti-aligned mode as it is generated, we measure the crosstalk at the power meters at the output ports. The measurement of each OAM mode (each vortex plate) contributes to one row in the crosstalk matrix Fig. 8. The crosstalk are normalized per row, so that all diagonal elements are 0 dB.

We measured lower crosstalk with high order modes. The crosstalk for low order modes (5AA, 6AA and 7AA) is higher;
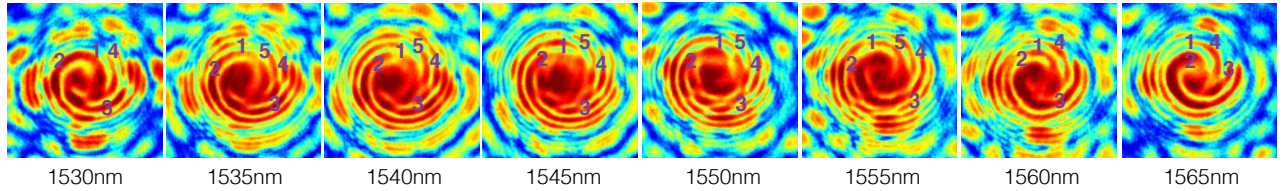
Fig. 10: Interferogram for OAM-5 over C-band. Five clear spirals appear from 1535 nm to 1555 nm.

topological charge. The figures are annotated to identify the five spiral arms.

For wavelengths from 1535 nm to 1555 nm the spiral arms are easily distinguishable and occur in similar positions. For wavelength below 1535 nm and above 1555 nm, the spiral arms deteriorate to only four being distinguishable. We demonstrated in [20] that we can retune the phase and amplitude correction to achieve good performance for any wavelength in the C-band. However, the bandwidth of the multiplexer for one tuning of the amplitude and phase is about 20 nm.

VII. DISCUSSION

The limiting factor of our tuning process is the system uncertainty, mostly the setup uncertainty against thermal effects. For the calibration of one circular polarization, the 27 VOAs consume about 2W of power; sweeping the 27 phase shifters requires another 1W. The tuning efficiency can be improved by using suspended silicon waveguide structure [21]. We prepared a robust heat sink for our packaged assembly. We integrated a temperature sensor to monitor the chip temperature while tuning. During the phase calibration, as we sweep the voltage on the phase shifter, the temperature of the tuned waveguide can change up to $40°$C and is constantly varying.

We use a Peltier cooler to drain heat toward the heat sink when the temperature rises, and stabilize the chip around room temperature. Nevertheless, a local temperature change, not necessarily large enough to cause detectable chip temperature rise, can cause beam shifts that lead to misalignment. A packaging plan with improved heat dissipation, or with OAM fiber coupling at the antenna array, can reduce system uncertainty and accommodate better calibration accuracy.

Our device generates circularly polarized OAM beams that can steadily propagate in OAM fiber, yet mode size conversion is still needed to match OAM fiber geometry [4]. The core of the OAM fibers is of 10 μm scale, while the diameter of our antenna array is 170 μm. With a silicon nitride-on-silicon platform, a multi-layer antenna array can be designed to shrink the size of the generated OAM modes [22]. Photonic wire bonds could also be used to close the gap between mode sizes through packaging [23]. The possibility of designing non-vertical emission antennas to favor the coupling to OAM fiber can also be investigated.

VIII. CONCLUSION

We design and characterize an optical phased array on a SOI platform that directly generates and multiplexes circularly polarized OAM modes with a very large channel number. The

device benefits from an intensity tuning circuit and achieves record low worst-case crosstalk (-17.2 dB) on a single OAM mode (OAM10). We measured -12 dB worst-case crosstalk from OAM5 to OAM11. The device supports 46 data channels (23 in each circular polarization), significantly extending the capacity of previous WDM-compatible silicon-based OAM multiplexers. The device provides a scalable, integrated solution for OAM generation and multiplexing in ultra-high capacity SDM systems.

APPENDIX A
OPTIMIZATION FLOWCHART

The flow chart of the alignment and optimization cycle is summarized in Fig. 11. We first set the wavelength-under-test on the laser. For amplitude tuning, we generate OAM0 mode with our device and record the camera image following path in Fig. 4. We perform intensity tuning based on the camera observations. The intensity profile appears as 27 individual spots. We integrate the power in each spot and identify the minimum power across the spots. We apply attenuation at each spot to achieve the minimum power. The tuning signal for attenuation is calculated based on the target attenuation in that path and the characterized response of the corresponding VOA. We iterated 30 times to achieve the reported intensity distribution.
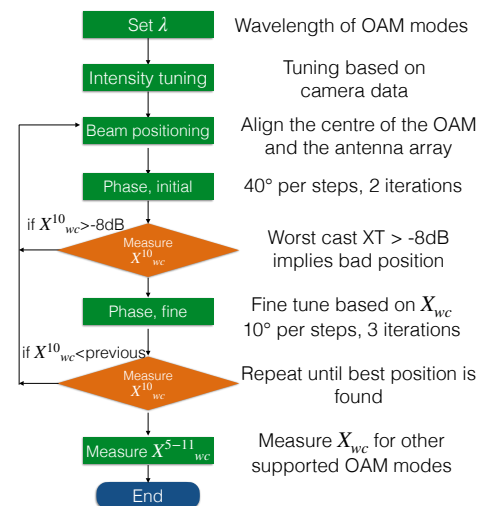

Fig. 11: Flow chart of optimization procedure in chip characterization.

For phase tuning, we switch to DEMUX configuration seen in Fig. 6. We generate OAM10 via a vortex plate and align
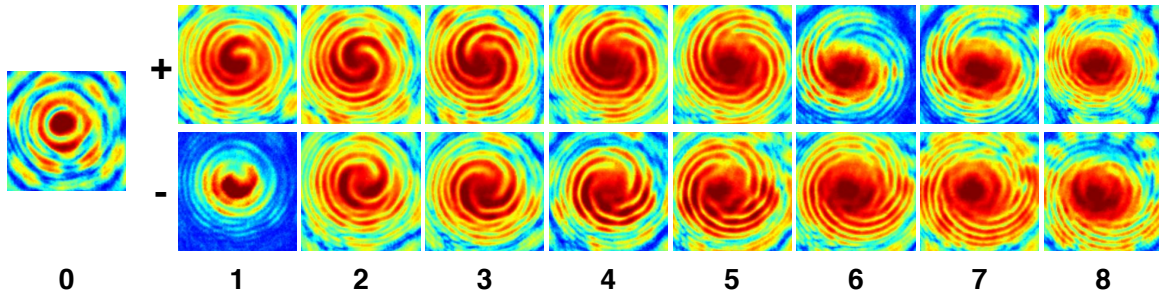
Fig. 12: Measured interference pattern for OAM-8 to OAM+8, number of spirals indicate topological charge.

it with our antenna array. The device demultiplexes OAM10 and we monitor 27 OAM mode output channels. If the phase of the device is well calibrated, we expect to see very little power on outputs other than the OAM10 output port.

In each iteration, we sweep the 27 phase tuning signals in sequence to improve the worst-case crosstalk on OAM10, i.e., X_{wc}^{10}. The power in any output port see contributions from all 27 paths. Sweeping one phase tuning signal will create a sinusoidal response in all output ports. We find the voltage that minimizes the worst-case crosstalk during one sweep, and we update the optimized tuning signal before the sweep of the next path. The optimized worst-case crosstalk after a two-iteration tuning gives a measure of the alignment quality between free-space optics and chip. If worst-case crosstalk is greater than -8 dB after the second iteration, realignment is needed. We chose a 40° tuning resolution during this coarse alignment for reasonable completion time.

Another three iterations performed for precise alignment before finally measuring crosstalk. The phase tuning resolution is reduced to 10° for precise alignment. We observed good convergence to an optimum set of tuning signals after the phase tuning with fine resolution. The time it takes to conduct phase tuning for one alignment condition is eight hours and is mainly consumed by the data communication among instruments. As the response time of the thermal phase shifter is in micro seconds, the phase tuning time in principle can be suppressed to less than a minute. We continue to make adjustments on the alignment until the optimal worst-case crosstalk is acquired for OAM10. We measured the performance for OAM5 to OAM11 at 1540 nm wavelength to build the crosstalk matrix in Fig. 8.

APPENDIX B
INTERFERENCE PATTERN FOR SUPPORTED OAM MODES

We show the interference patterns from -8 to +8 measured at 1540 nm in Fig. 12. The origin of the spiral is closer to the center at lower order OAM, just as we expect from our simulations. The diameter of the generated beam grows as the topological charge of the OAM mode increases, while the size of the reference Gaussian remains the same. This makes the spiral arms for high order modes like OAM±8 less distinguishable; there is less overlap between the generated beam and reference Gaussian. For this reason we did not capture interferograms of OAM9 and beyond. The backgrounds for

OAM-1 and OAM+6 are more blue; we suspect the fiber-to-chip couplers involved in their generation are more lossy.

REFERENCES

[1] W. Shi, Y. Tian, and A. Gervais, "Scaling capacity of fiber-optic transmission systems via silicon photonics," *Nanophotonics*, vol. 9, no. 16, pp. 4629–4663, 2020.

[2] P. J. Winzer, D. T. Neilson, and A. R. Chraplyvy, "Fiber-optic transmission and networking: the previous 20 and the next 20 years," *Optics express*, vol. 26, no. 18, pp. 24 190–24 239, 2018.

[3] P. J. Winzer and D. T. Neilson, "From scaling disparities to integrated parallelism: A decathlon for a decade," *Journal of Lightwave Technology*, vol. 35, no. 5, pp. 1099–1115, 2017.

[4] M. Banawan, S. K. Mishra, A. Gouin, N. Bacon, X. Guan, L. Wang, S. LaRochelle, and L. A. Rusch, "Expanded modal capacity for OAM with standard 2×2 MIMO," in *2022 European Conference on Optical Communication (ECOC)*. IEEE, 2022, pp. 1–4.

[5] Y. Ohtake, T. Ando, N. Fukuchi, N. Matsumoto, H. Ito, and T. Hara, "Universal generation of higher-order multiringed laguerre-gaussian beams by using a spatial light modulator," *Optics letters*, vol. 32, no. 11, pp. 1411–1413, 2007.

[6] M. Massari, G. Ruffato, M. Gintoli, F. Ricci, and F. Romanato, "Fabrication and characterization of high-quality spiral phase plates for optical applications," *Applied Optics*, vol. 54, no. 13, pp. 4077–4083, 2015.

[7] E. Karimi, B. Piccirillo, E. Nagali, L. Marrucci, and E. Santamato, "Efficient generation and sorting of orbital angular momentum eigenmodes of light by thermally tuned q-plates," *Applied Physics Letters*, vol. 94, no. 23, p. 231124, 2009.

[8] X. Cai, J. Wang, M. J. Strain, B. Johnson-Morris, J. Zhu, M. Sorel, J. L. O'Brien, M. G. Thompson, and S. Yu, "Integrated compact optical vortex beam emitters," *Science*, vol. 338, no. 6105, pp. 363–366, 2012.

[9] S. Li, Z. Nong, X. Wu, W. Yu, M. He, C. Klitis, Y. Zhu, S. Gao, J. Liu, Z. Li *et al.*, "Orbital angular momentum vector modes (de) multiplexer based on multimode micro-ring," *Optics express*, vol. 26, no. 23, pp. 29 895–29 905, 2018.

[10] N. Zhou, S. Zheng, X. Cao, S. Gao, S. Li, M. He, X. Cai, and J. Wang, "Generating and synthesizing ultrabroadband twisted light using a compact silicon chip," *Optics Letters*, vol. 43, no. 13, pp. 3140–3143, 2018.

[11] N. Zhou, S. Zheng, X. Cao, Y. Zhao, S. Gao, Y. Zhu, M. He, X. Cai, and J. Wang, "Ultra-compact broadband polarization diversity orbital angular momentum generator with 3.6× 3.6 µm2 footprint," *Science advances*, vol. 5, no. 5, p. eaau9593, 2019.

[12] T. Su, R. P. Scott, S. S. Djordjevic, N. K. Fontaine, D. J. Geisler, X. Cai, and S. Yoo, "Demonstration of free space coherent optical communication using integrated silicon photonic orbital angular momentum devices," *Optics express*, vol. 20, no. 9, pp. 9396–9402, 2012.

[13] B. Guan, C. Qin, R. P. Scott, N. K. Fontaine, T. Su, R. Proietti, and S. Yoo, "Polarization diversified integrated circuits for orbital angular momentum multiplexing," in *2015 IEEE Photonics Conference (IPC)*. IEEE, 2015, pp. 649–652.

[14] Y. Chen, L. A. Rusch, and W. Shi, "Silicon photonic integrated circuits for oam generation and multiplexing," in *Silicon Photonics for High-Performance Computing and Beyond*. CRC Press, 2021, pp. 249–263.

[15] Y. Chen, Z. Lin, S. Bélanger-de Villers, L. A. Rusch, and W. Shi, "Wdm-compatible polarization-diverse oam generator and multiplexer in silicon photonics," *IEEE Journal of Selected Topics in Quantum Electronics*, vol. 26, no. 2, pp. 1–7, 2019.

[16] Y. Chen, L. A. Rusch, and W. Shi, "Integrated circularly polarized oam generator and multiplexer for fiber transmission," *IEEE Journal of Quantum Electronics*, vol. 54, no. 2, pp. 1–9, 2017.

[17] C. Brunet, P. Vaity, Y. Messaddeq, S. LaRochelle, and L. A. Rusch, "Design, fabrication and validation of an oam fiber supporting 36 states," *Optics express*, vol. 22, no. 21, pp. 26 117–26 127, 2014.

[18] E. Kleijn, M. K. Smit, and X. J. Leijtens, "New analytical arrayed waveguide grating model," *Journal of lightwave technology*, vol. 31, no. 20, pp. 3309–3314, 2013.

[19] N. Zhang, M. Scaffardi, C. Klitis, M. N. Malik, V. Toccafondo, F. Fresi, J. Zhu, X. Cai, S. Yu, A. Bogoni *et al.*, "Large-scale integrated reconfigurable orbital angular momentum mode multiplexer," *arXiv preprint arXiv:2008.00680*, 2020.

[20] Y. Chen, S. Levasseur, L. A. Rusch, and W. Shi, "Integrated phased array for circularly polarized oam multiplexing," in *2022 The European Conference on Optical Communication (ECOC)*, 2022.

[21] K. Chen, F. Duan, and Y. Yu, "High-performance thermo-optic tunable grating filters based on laterally supported suspended silicon ridge waveguide," *Optics express*, vol. 26, no. 15, pp. 19 479–19 488, 2018.

[22] W. D. Sacher, Y. Huang, G.-Q. Lo, and J. K. Poon, "Multilayer silicon nitride-on-silicon integrated photonic platforms and devices," *Journal of lightwave technology*, vol. 33, no. 4, pp. 901–910, 2015.

[23] P.-I. Dietrich, M. Blaicher, I. Reuter, M. Billah, T. Hoose, A. Hofmann, C. Caer, R. Dangel, B. Offrein, U. Troppenz *et al.*, "In situ 3d nanoprinting of free-form coupling elements for hybrid photonic integration," *Nature Photonics*, vol. 12, no. 4, pp. 241–247, 2018.

Leslie A. Rusch (S'91-M'94-SM'00-F'10) received the B.S.E.E. degree (with honors) from the California Institute of Technology, Pasadena, CA, USA, in 1980 and the M.A. and Ph.D. degrees in electrical engineering from Princeton University, Princeton, NJ, in 1992 and 1994, respectively. She holds a Canada Research Chair in *Communications Systems Enabling the Cloud*, is a full Professor in the ECE Department at Université Laval, QC, Canada, where she is also a member of the Centre for Optics, Photonics, and Lasers (COPL). She has experience in defense, industrial, and academic communications research. She was a communications project engineer for the Department of Defense from 1980–1990. While on leave from Université Laval, she spent two years (2001–2002) at Intel Labs creating and managing a group researching new wireless technologies. Prof. Rusch performs research on wireless and optical communications. Her research interests include digital signal processing for coherent detection in optical communications, spatial multiplexing using orbital angular momentum modes in fiber, radio over fiber, and OFDM for passive optical networks; and in wireless communications, optimization of the optical/wireless interface in emerging cloud based computing networks, and implantable medical sensors with high bit rate UWB telemetry. She is recipient of the IEEE Canada Fessenden Award for Telecommunications research, and the IEEE Canada J. M. Ham Award for Graduate Supervision. Prof. Rusch has published over 130 journal articles in international journals (90% IEEE/IEE) with wide readership, and contributed to over 165 conferences. Her articles have been cited over 5100 times per Google Scholar.

Yuxuan Chen was born in Wuhan, China, in 1992. He received his B.S. degree in Opto-Information Science and Technology from Huazhong University of Science and Technology, Wuhan, China in 2014. He is currently working toward his Ph.D. degree at the Department of Electrical and Computer Engineering, Université Laval, Québec, QC, Canada. His research interests include photonic integrated circuit design, orbital angular momentum of light, and space division multiplexing systems.

Wei Shi (S'07–M'12-SM'22) is a professor with the Department of Electrical and Computer Engineering, Université Laval, Québec, Canada and holds a Canada Research Chair in Silicon Photonics. He received the Ph.D. degree in Electrical and Computer Engineering from the University of British Columbia, Vancouver, Canada in 2012. He was a postdoctoral researcher at McGill University, Montreal, QC, Canada in 2013, where he held a Postdoctoral Fellowship from the Natural Sciences and Engineering Research Council of Canada (NSERC). His research focuses on integrated photonic devices and systems, involving silicon photonics, nanophotonics, CMOS- photonics co-design, high-speed optical communications, hybrid photonic integration, and optical sensors. He is a faculty member of the Center for Optics, Photonics (COPL) and Senior Member of Optica.

Simon Levasseur received his DEC degree in physic technology from the La Pocatière Cégep. Before joining University Laval in 2018, he has been working with optical interferometric, cryogenic vacuum systems and others technology for Telops RD department. While he was working for AiWorks, he learned how to make good use of AI to achieve the best benefit out of it. His research interest include photonics integrated circuit packaging, both optical and electrical. Ultimate goal: Being the best lab mentor to teach good lab practice for security, protocol elaboration and risks mitigation.